Aalborg Universitet

Aalborg University

DENMARK

Determine stormwater pond geometrics and hydraulics using remote sensing technologies: a comparison between airborne-LiDAR and UAV-photogrammetry field validation against RTK-GNSS

Zhao, Guohan; Rasmussen, Michael R.; Larsen, Kim Guldstrand; Srba, Jiri; Nielsen, Thomas Dyhre; Goorden, Martijn; Qian, Weizhu; Nielsen, Jesper Ellerbæk

Determine stormwater pond geometrics and hydraulics using remote sensing technologies: A comparison between airborne-LiDAR and UAV-photogrammetry field validation against RTK-GNSS

Guohan Zhao [a,*], Michael R. Rasmussen[a], Kim G. Larsen[b], Jiri Srba[b], Thomas D. Nielsen[b], Martijn A. Goorden[b], Weizhu Qian[b] and Jesper E. Nielsen[a]

[a] Department of Built Environment, Aalborg University, Thomas Manns Vej 23, Aalborg Øst 9220, Denmark
[b] Department of Computer Science, Aalborg University, Selma Lagerlöfs Vej 300, Aalborg Øst 9220, Denmark
*Corresponding author. E-mail: zhaoguohan2014@hotmail.com

GZ, 0000-0003-1793-9519

ABSTRACT

Flow-regulated stormwater ponds providing safe outflow discharges prevail as the primary stormwater management tool for stream protections. Detailed pond geometries are essential metrics in pond monitoring technologies, which convert the point-based water level measurements to areal/volumetric ponding water estimations. Unlike labour-intensive surveys (e.g., RTK-GNSS or total stations), UAV-photogrammetry and airborne-LiDAR have been advocated as cost-effective alternatives to acquire high-quality datasets. In this paper, we compare the use of these two approaches for stormwater pond surveys. With reference to RTK-GNSS *in-situ* observations, we identify their geometric and hydraulic discrepancies based on six stormwater ponds from three aspects: (i) DEMs, (ii) stage-curves and (iii) outflow discharges. Three main findings are outlined: (i) for wet ponds where moisture environments are dominant, UAV-photogrammetry outperforms (infrared) airborne-LiDAR, where airborne-LiDAR yields 0.15–0.54 $NSE_{outflow}$, which is unacceptable; (ii) for dry ponds, UAV-photogrammetry obtains 0.88–0.89 $NSE_{outflow}$ as poor vegetation penetrations; two correction methods (i.e., grass removal and shifted stage-curves) are proposed, indicating good alignment to RTK-GNSS observations and (iii) UAV-photogrammetry delivers <0.1 m resolution in outlining break-line features for stormwater pond structures. With significant economic advantages, the multi-UAV collaborative photogrammetry would address the shortcomings of a single UAV and thus pave the way for large urban catchment/watershed survey applications.

Key words: airborne-LiDAR, outflow discharges, stormwater ponds geometrics, stream protections, structure from motion, unmanned aerial vehicles

HIGHLIGHTS

- UAV-photogrammetry outperforms airborne-LiDAR in wet ponds.
- UAV-photogrammetry yields underwater elevations and is insensitive to groundwater variations.
- UAV-photogrammetry does not perform so well as airborne-LiDAR in dry ponds.
- The proposed two correction methods resolve vegetation errors well in UAV-photogrammetry.
- The multi-UAVs collaborative photogrammetry has the potential to address identified shortcomings.

GRAPHICAL ABSTRACT
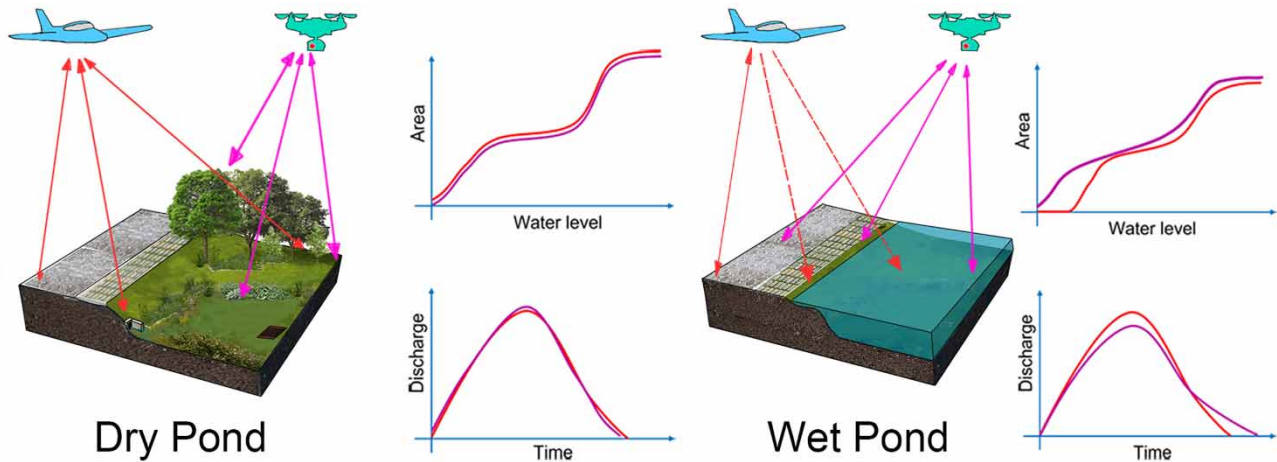
1. INTRODUCTION

Urbanizations with increased impervious areas and reduced infiltrations intensify human interferences towards the urban hydrological cycle, which poses substantial threats towards stream ecosystems, including flood risks (Hundecha & Bárdossy 2004; Suriya & Mudgal 2012), water-quality degradations (Liu *et al.* 2019a, 2019b), and stream channel erosions (Arnold & Toran 2018). To mitigate these side-effects, flow-regulated stormwater ponds with active/passive flow actuators (e.g., valves, gates and pumps) providing safe outflow discharges towards streams have been considered as a feasible solution to protect stream ecosystems. As the primary stormwater management tool, stormwater ponds can be classified into dry and wet ponds, and both ponds provide extended storage volumes as well as regulated outflow discharge towards streams (Emerson *et al.* 2005). During extreme precipitations, these stormwater ponds delay and reduce the flood peak flow downstream, and thus protect the stream from erosion with the reduced hydraulic peak loads. During dry weather, wet stormwater ponds maintain surface water at a constant level, also referred as to 'constant storage volume'. This detention process provides sufficient residence time allowing for sedimentation, thereby resulting in degraded organic matters, such that debris and other pollutants are reduced as much as possible before the next discharge.

Pond discharge monitoring is critical for quantifying the associated hydraulic loads and evaluating their pollutant-removal performances. Regardless of different regulation devices in various local conditions, Thomsen (2019) proposed a measuring method that can convert water level measurements into discharges. This approach demonstrates a cost-effective monitoring approach addressing the demands of the installation of many real-time sensors at multiple sites among large-scale real-time stormwater control systems. However, prior knowledge of detailed stormwater pond geometries is required for this method. Furthermore, according to Li (2020), construction errors, post-construction, sedimentations and erosions can change pond geometries considerably over the years, which further results in degraded pollutant-removal capabilities and weakened flood mitigation capabilities. Hence, cost-effective, accurate and timely survey technologies are needed to obtain updated *in-situ* stormwater pond geometry.

As opposed to the labor-intensive *in-situ* surveys using Real-Time Kinematic positioning Global Navigation Satellite Systems (RTK-GNSS) or total stations (Bandini *et al.* 2020), remote sensing technologies, including manned aircraft and unmanned aerial vehicles (UAVs) mounted with various sensors (e.g., RGB camera and light detection and ranging), have been advocated as superior survey options to acquire high-resolution datasets concerning geological and hydrological surveys. This includes, for instance, vegetation/soil observations (Geipel *et al.* 2014), forestry surveys (Chou *et al.* 2010; Wallace *et al.* 2012), disaster monitoring (Dominici *et al.* 2012; Chen *et al.* 2014) and fluvial morphological changes monitoring (Flener *et al.* 2013; Eltner *et al.* 2015; Tamminga *et al.* 2015a, 2015b; Langhammer & Vacková 2018). Recently, their applications have been expanded towards urban water fields including flow velocimetry (Kääb & Leprince 2014; Perks *et al.* 2016), overland flow modelling (Leitão *et al.* 2016; Zhao *et al.* 2022), urban flood mapping (Feng *et al.* 2015; Gebrehiwot & Hashemi-Beni 2020, 2021) and flood risk assessments (Rivas Casado *et al.* 2018; Karamuz *et al.* 2020; Li *et al.* 2021; Trepekli *et al.* 2022).

To identify a cost-effective remote sensing technology that reveals stormwater pond geometries in detail, we compared airborne-LiDAR and UAV-photogrammetry technologies, taking RTK-GNSS as the references. To reveal their discrepancies, we first compared the geometric accuracy in terms of Digital Elevation Models (DEMs) and stage-curves. Then, we further distinguished their hydraulic impact towards outflow discharges. Six stormwater ponds of different sizes, types (i.e., dry/wet), vegetation statuses and catchment characteristics were selected as study cases.

2. MATERIALS AND METHODS

2.1. Selected stormwater ponds

We chose a Danish site called 'Sønder Tranders' in Northern Jutland, see Figure 1. Accounting for various pond sizes, pond types (wet/dry), vegetation statuses and service catchment characteristics, six stormwater ponds in this site were selected, see Table 1.

2.2. UAV-photogrammetry

UAVs, which refer to lightweight aircraft operated without human pilots onboard, have been advocated as a preferential remote sensing option (Bandini *et al.* 2020). In contrast to orbital satellites or manned aircraft, UAVs involve considerably lower costs while offering flexible options (i.e., flight time schedules, weather conditions, observation altitudes and speeds) and acquiring centimeter resolution accuracies (Pajares 2015). With low-cost deployments, UAVs can revisit the same site frequently, thus being better at capturing the temporally dynamic changes, particularly for small objects (e.g., streams and ponds). In this study, we selected the DJI Mini 2 (DJI, China 2021), see Supplementary Figure A1. This platform is a foldable quadcopter Mini-UAV, and weights 249 g including the three components for the photogrammetry: (i) a 4K high-resolution RGB image sensor (i.e., 12 million Pixel 1/2.3″ frame size CMOS) capturing $4,000 \times 2,250$ 72 dpi resolution images; (ii) a 3-axis gimbal (i.e., tilt, roll and pan) providing sensor stabilizations concerning turbulence conditions and (iii) the wind resistance ability (i.e., 8.5–10.5 m/s wind speeds) gaining successful high-quality image acquisitions.

The structure from motion (SfM) approach was applied, which is the construction of the 3D scene from multiple pictures of the same feature taken in various angles merely by moving around the image sensor (Ullman 1979). SfM resolves the camera positions and orientations automatically without prior knowledge of the poses and 3D locations of the camera, and is thus considered to be a low-cost, effective tool for many geoscience applications (Lowe 1999; Westoby *et al.* 2012). However, without direct georeferencing the scale and orientation to the true absolute coordinates, 3D point clouds from SfM reflect a relative 'image-space' coordinate system, only. To align such datasets to the real-world, ground control points (GCPs) are required.

We conducted 18 flights at three flight altitudes (i.e., 20, 40 and 60 m) in the weather conditions either sunny days or overcasting days. According to Leitão *et al.* (2016), low-altitude flights distinguish high-quality details with small ground sampling distances (GSDs). However, to reach the same degree of image overlapping as the high-altitude flights, the low-altitude flights must incorporate more photos, thus boosting SfM computation significantly (e.g., big Ponds 5 and 6). Otherwise, the poor overlapping images result in numerous void cells due to image miss-matching (Supplementary Figure A2). Hence, UAV-photogrammetry in the flight altitude of 60 m was selected. Based on Agüera-Vega *et al.* (2017a, 2017b), 15 GCPs were chosen for calibrations thus ensuring high horizontal and vertical accuracy. Agisoft Metashape Professional (version 1.7.2) was used to perform SfM, where the default settings were used (Agisoft Metashape User Manual 2021). Detailed flight parameters, GCP locations, image overlapping and SfM processing time are provided in Supplementary A. The GCPs for UAV-photogrammetry were collected using the RTK-GNSS presented in Section 2.4.

2.3. Airborne-LiDAR

Airborne light detection and ranging, also referred to as airborne laser scanning (ALS), provides high-density and high-accuracy 3D point cloud dataset acquisitions. With direct georeferencing techniques, it generates a cloud of laser range measurements, thus intuitively reflecting detection objects in three-dimensional coordinates (Liu 2008; Yan *et al.* 2015). With a strong penetration capacity, LiDAR can measure the profile of the terrain suppressing the vegetation interference. So, airborne-LiDAR has been acknowledged as a cost-effective solution for obtaining large-scale terrain survey and forest survey applications, as well as input for urban flood modelling, for instance: DEMs generations (Liu 2008), forest structure mapping (Hopkinson 2007), 3D building modelling (Wang 2013) and urban flood modelling (Mason *et al.* 2007; Tsubaki & Fujita 2010; Balstrøm & Crawford 2018; Zhao *et al.* 2021).
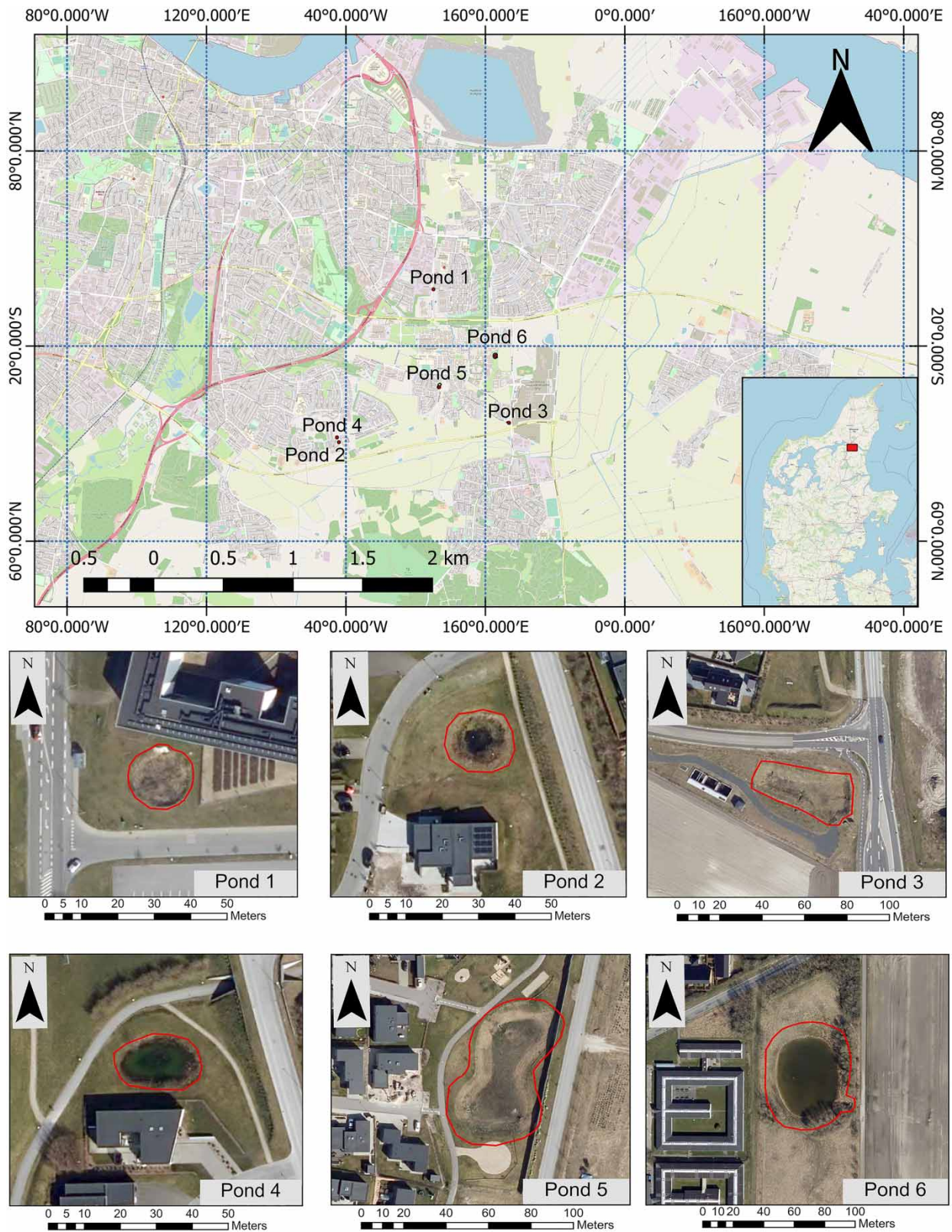
Figure 1 | The location of 'Sønder Tranders' in Northern Jutland of Denmark and aerial images for six stormwater ponds. Base map is available from OpenStreetMap (Maps.stamen.com 2021) and GeoDenmark orthophoto 2020 (SDFE 2020).

Table 1 | General geographic information table for six stormwater ponds

Pond No.	Area (m²)	Volume (m³)	Pond type	Service catchment type	Elevations (m)	Slopes (%)	Vegetation status	Max. elevation (m)	Mini. elevation (m)	Constant water levels (m)
1	249	325	Dry	Commercial/ Parking lot	15.68 ± 0.53	23.13 ± 19.92	High	16.88	14.69	×
2	266	185	Wet	Residential	20.19 ± 0.24	8.98 ± 6.76	Low	20.82	19.90	19.90
3	986	2,000	Dry	Residential/ Expressway	9.47 ± 0.99	28.11 ± 18.37	Medium	11.55	7.86	×
4	305	150	Wet	Residential	22.44 ± 0.19	6.64 ± 6.99	Low	22.91	22.2	22.29
5	2,679	3,200	Dry	Residential/ Expressway	13.44 ± 0.57	12.06 ± 9.04	Low	14.89	12.73	×
6	3,527	9,500	Wet	Commercial/ Expressway	11.87 ± 0.63	8.97 ± 11.03	High	14.75	11.0	11.41

Note: Elevations and slopes were calculated based on the ground RTK-GNSS, and the vegetation status was determined based on the *in-situ* observations.

In Denmark, the aerial observations of airborne-LiDAR were carried out by the Danish Agency for Data Supply and Efficiency (SDFE 2021a, 2021b) via the Danish Basic Data Program 2021. The nationwide airborne scanning task of LiDAR cloud points was collected by four aeroplanes from the years 2014 to 2015 in three leaf-off seasons (i.e., autumn 2014, spring and autumn 2015) on cloud-free days. The LiDAR sensors mounted on these aeroplanes mainly include a RIEGL VQ-780i sensor, supporting multiple target detections in various environments, ultra-wide area/height detections and ultra-high point density mapping (e.g., 2.66 million points/second). In this way, the point density of >4 ppm^2 was strictly controlled on the overall dataset. Besides, in order to fit for the specific purpose of the long-range aerial topographic scanning task other than the bathymetry survey, LiDAR sensors were performed at infrared spectrum (i.e., 1,550 nm wavelength) thus obtaining surface terrain measurements with good penetration to atmospheric haze, dust, and vegetation at relatively low costs. For the same reason, the presented LiDAR results in this study are referring to the infrared-LiDAR unless specified in bathymetric/green-beam LiDAR. After calibration against GCPs, vertical accuracy of <6 cm and horizontal accuracy of <15 cm are ensured according to DEM product specification v1.0.0 (SDFE 2020). However, due to excessive expenses, the national LiDAR cloud points have only been updated every 5 years since 2018. In this study, the airborne-LiDAR cloud point blocks covering the six ponds were collected from the 2-day flight tasks on April 5th and 6th, 2015 and the next LiDAR scanning is scheduled for 2023.

2.4. Ground RTK-GNSS validations

We conducted *in-situ* observations using the Leica Viva GNSS GS08 receiver setup (Leica Geosystems 2021), which is considered as the benchmarking results. This setup consists of three components: Leica Viva CS10 field controller, GLS 30 pole and GS08 antenna, see Supplementary Figure B. RTK-GNSS provides centimetre-level accuracy (Horizontal: 5 mm; Vertical: 10 mm). In our field works, the point-wise measurement uncertainty was controlled to be less than 2 cm. By employing 1 m-resolution rectangular grids for RTK-GNSS point positioning, a 1–2 ppm^2 density was ensured for RTK-GNSS datasets (see Supplementary Figure B).

2.5. Data processing and comparison experiment designs

The general data processing was carried out following four steps, see Figure 2. The pond datasets collected from the three survey technologies were stored as LiDAR point clouds in LAS file formats. The raw LiDAR point cloud datasets were pre-processed by Danish Agency for Data Supply and Efficiency. The classification was conducted using Rapidlasso's LAS-tools software, where 11 LAS classes (i.e., ground, water, vegetations, buildings, roads, railways, bridges, power lines, construction cranes, other surfaces, and noise/artifacts) were divided. Besides, to denoise LiDAR datasets, the voxel grid filter was applied to remove for instance, bird flocks. Furthermore, the data quality control was performed by having expert inspections as well as by validating against the other support geodata layers (e.g., ortho imagery, topographic map, building footprint/roads vectors and water body vectors). To convert them into DEMs, we used the ArcGIS' Make LAS
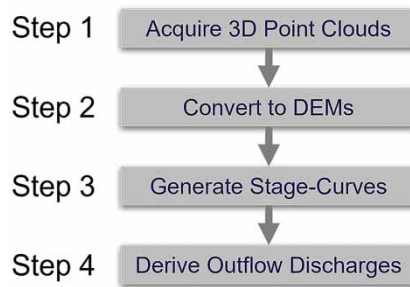
Figure 2 | General workflow, where shaded grey boxes illustrate the steps for data processing.

Dataset Layer tool to extract the LAS points belonging to the specific laser returns (i.e., first/last return for extracting non-ground/ground points). Here, LiDAR DEMs were derived from the last return laser pulse only, thereby excluding vegetation elevations in stormwater ponds. Then, ArcGIS' LAS Dataset to Raster tool converted 3D point clouds into DEMs (i.e., digital surface models/digital terrain models). Thereafter, the stage-curves were generated from DEMs based on a Python customized script. This algorithm, also referred as to 'multilevel slicing volumetric analysis' (Liu *et al.* 2010; Wang & Yu 2012), iteratively computes the water areas/volumes for each step when increasing the water level at a constant incremental, the process of which starts from the specified minimum elevation value until the specified maximum elevation value is reached. With pond geometries described by stage-curves, outflow discharges were derived from the Storm Water Management Model (SWMM), accounting for catchment inflows.

According to the workflow, the UAV-photogrammetry datasets were compared to the airborne-LiDAR ones at four levels: (i) 3D point clouds comparison, where discrepancies in point-wise accuracy were identified; (ii) DEMs comparison, where void cells and cell elevation accuracy were investigated; (iii) stage-curve comparison, where volumetric discrepancies were addressed and (iv) outflow discharges, where hydraulic performance discrepancies were emphasized. As suggested by Section 2.4, RTK-GNSS obtains the highest measurement accuracy, and therefore, its associated products were all taken as consistent references. The 3D point cloud comparisons and their corresponding results are presented in Supplementary Figure C.

To maintain consistency, DEMs comparisons were conducted as follows. Firstly, we employed 1-m rectangular grids as the consistent grids to collect the elevation samples from all three 3D point cloud datasets. Secondly, the average was applied as the aggregation method to determine the cell values in DEMs. Lastly, we deliberately kept the void values in DEM without applying extrapolation methods, such that 'out-of-reach' spots due to the differences in using active/passive sensors could be identified and further discussed. For elevation difference comparisons, the vertical discrepancies in DEMs were computed by subtracting RTK-GNSS DEMs from the DEMs derived from the other two approaches. Here, the comparison extent was kept identical based on the intersection of comparison datasets, thereby excluding void cells.

The water stage–areas/volumes curves, also referred to as 'stage-curves', describe the relationship between water surface areas/water volumes and the water levels in ponds. Water level gauges can retrieve water level variations cost-effectively, therefore, stage-curves are used to translate the current water surface areas/water volumes based on the measured water level. To maintain comparison consistency, we used identical minimum elevations and identical maximum elevations sampled from the six ponds using RTK-GNSS, see Table 1. In addition, the identical incremental value of 2 cm was used. Due to volumetric computations, void cells in DEMs are considered as occupied volumes in the algorithm, and are thus excluded from volumetric estimations. To avoid this, three types of void cells were classified: (i) void cells in LiDAR DEMs due to miss-reflections from surface water; (ii) void cells in UAV-photogrammetry DEMs due to shaded areas; (iii) void cells in ground RTK-GNSS DEMs due to the territorial accessibility issues (e.g., access to water surfaces and high vegetations). So, the void cells (i) and (iii) (water surfaces) for water surface areas were first filled up by assigning constant water level values sampled from the lowest adjacent 'water-edge interface' elevations (Bandini *et al.* 2020). Then, the void cells (ii) and (iii) (vegetations) were patched by assigning averaged elevation values based on their neighbouring cells.

To identify stormwater pond hydraulic discrepancies, three hydraulic models were established, corresponding to three stage-curves for each stormwater pond. The EPA-SWMM was used as the 1D hydrodynamic solver (Rossman 2007). These SWMM models consist of three components: (i) a service urban catchment for the inflow generations; (ii) a storage node representing stormwater pond geometries using stage-curves and (iii) an orifice component for outflow discharges.

The non-linear reservoir model was applied for inflow generations. Here, to pursue a fast urban catchment rainfall-runoff response, 100% impervious rate and 2% slope were applied. Without having detailed stormwater pond registrations, catchment sizes for six stormwater ponds were synthesized based on their measured volumes according to the Danish Intensity Duration Frequency (IDF) curves. The maximum depths (i.e., emergency overflows) for storage nodes and initial water levels (i.e., constant water levels) for wet ponds were determined by *in-situ* RTK-GNESS measurements in Table 1. SWMM's orifice provides adjustable opening settings which provide passive/active regulated outflow discharges (McDonnell *et al.* 2020). So, the orifice was selected as the outflow discharge function to derive the hydrographs. Here, the orifices adopted the circle geometry to mimic water break flow regulators, and their diameters were sized based on the maximum discharge regulated by the Danish Environmental Protection Act (Miljøstyrelsen 2019). In addition, a 5-year return period box rainfall, with a constant rainfall intensity of 0.9 μm/s continuing for 720 min, was synthesized. Its rainfall amounts were deliberately controlled at certain total volumes to fill above 90% of full capacities while having no overflows, such that pond geometric discrepancies can be reflected comprehensively by having a complete water level rising and recession process. Furthermore, simulated periods were intentionally extended sufficiently for all ponds to empty themselves, see Table 2.

2.6. Hydraulic metrics

To quantify the hydraulic discrepancies against the benchmark solution, we used Nash–Sutcliffe model efficiency coefficient (NSE) and root mean square error (RMSE) as the metrics:

$$NSE = 1 - \frac{\sum\limits_{t=1}^{T}(Q_{GNSS}^{t} - Q_{M}^{t})^2}{\sum\limits_{t=1}^{T}(Q_{GNSS}^{t} - \bar{Q}_{GNSS})^2}$$

$$RMSE = \sqrt{\frac{\sum\limits_{t=1}^{T}(D_{M}^{t} - D_{GNSS}^{t})^2}{T}}$$

where Q_{GNSS}^{t} is the simulated outflow discharge rate based on GNSS derived stage curves, Q_{M}^{t} is the simulated outflow discharge rate based on either UAV-photogrammetry or airborne-LiDAR stage curves. $\bar{Q}_{GNSS}$ is the mean of the outflow discharge rate based on GNSS derived stage curves. D_{GNSS}^{t} is the simulated water depth based on GNSS derived stage curves. D_{M}^{t} is the simulated water depth based on either UAV-photogrammetry or airborne-LiDAR stage curves.

3. RESULTS

3.1. DEM results and comparisons

The results from Ponds 2 and 5 were selected as representations of six ponds hereof, where detailed Pond 1–6 results are provided in Supplementary Figure D. Figure 3 illustrates the DEMs of Ponds 2 and 5 derived from UAV-photogrammetry, airborne-LiDAR and ground RTK-GNSS, respectively. In contrast to the 1 m resolution of ground RTK-GNSS, the other

Table 2 | SWMM model setup parameters

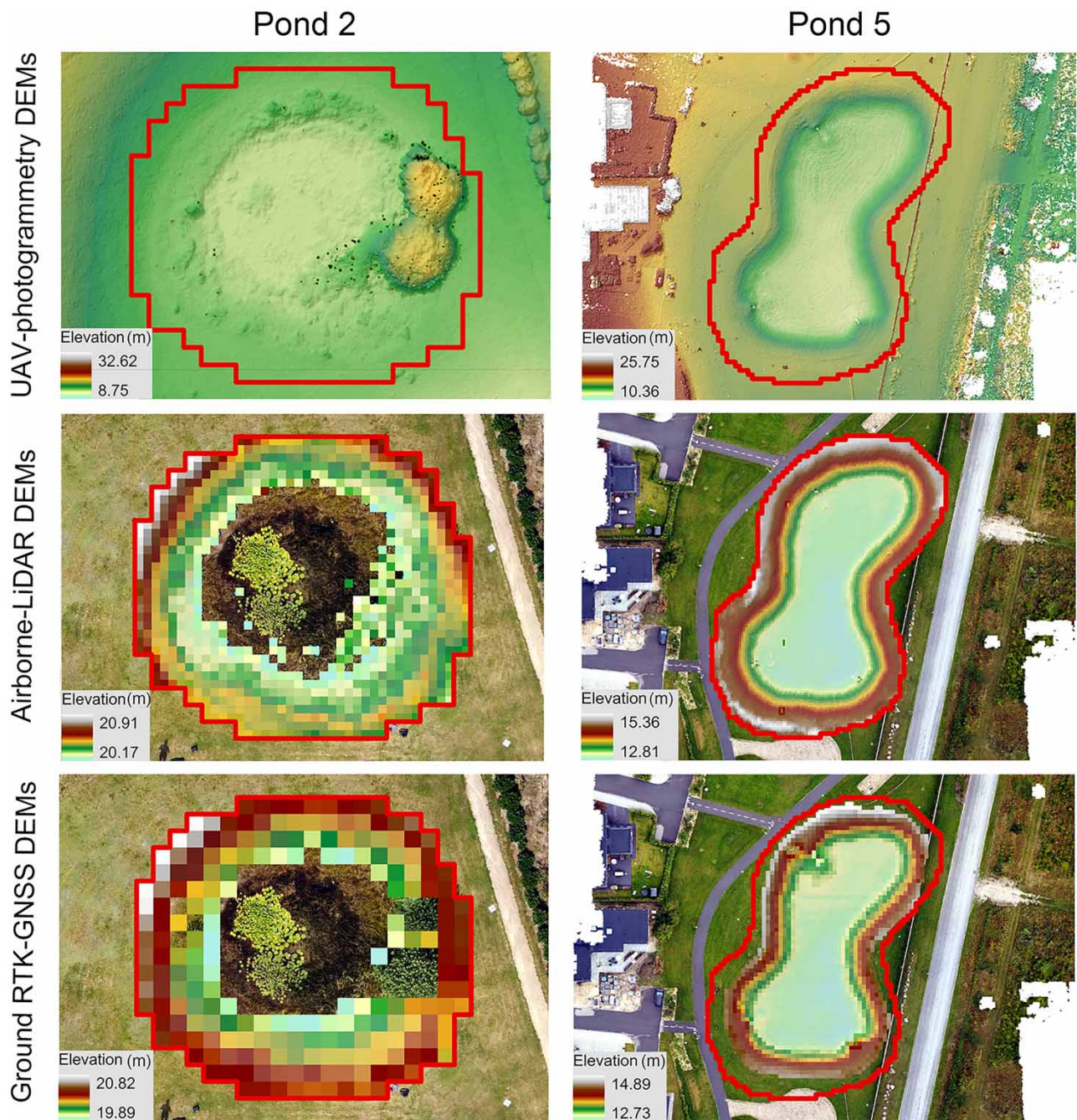| Pond ID	Impervious catchment area (ha)	Flow width (m)	Slope (%)	Max. depth (m)	Orifice diameters (m)	Max. discharge (L/s)	Simulated periods (days)
1	1.1	104.8	2	2.166	0.025	5	2
2	0.4	70.7	2	0.911	0.015	1	4
3	6	245	2	3.649	0.050	11	4
4	0.3	67	2	0.614	0.015	1	4
5	8.5	291.5	2	2.136	0.050	20	6
6	21	458.3	2	3.307	0.080	36	6

Figure 3 | DEM results obtained from UAV-photogrammetry (0.02 m), airborne-LiDAR (0.5 m) and ground RTK-GNSS (1 m) in Ponds 2 and 5, where red lines represent pond boundaries, and transparent pixels above the base map within boundaries represent for void cells. Please refer to the online version of this paper to see this figure in colour: https://dx.doi.org/10.2166/hydro.2023.178.

two approaches demonstrate considerably higher resolutions (i.e., 0.4 m for airborne-LiDAR and 0.02 m for UAV-photogram-metry), thus incorporating more details for the stormwater ponds with significantly higher point densities. Notably, with sub-centimeter resolution of <2 cm, the geometrics of three outflow structures for Pond 5 are clearly distinguished from the UAV-photogrammetry DEM. Here, UAV-photogrammetry demonstrates significant advantages over conventional topo-graphic technology (i.e., ground RTK-GNSS or total stations), whereas ground RTK-GNSS acquires higher point-wise accuracy of <2 cm. Besides this, substantial void cells were observed in RTK-GNSS observations spatially for Pond 3. This

is attributed to high vegetation statuses, constant surface water and sediments that present territorial barriers resulting in inaccessibility issues during the field works. In contrast, the UAV remote sensing technologies carrying out the *in-situ* aerial scanning from the air zone, show significant superiority. Nevertheless, the void cells were still observed in UAV-photogrammetry and airborne-LiDAR DEMs. Because of the absorption of laser backscatter from the surface water and the moisture regions (e.g., aquatic vegetations and saturated soils), void cells occur for the airborne-LiDAR in the case of Pond 2 (also Pond 4 in Supplementary Figure D). As opposed to airborne-LiDAR, UAV-photogrammetry did not encounter such issues and illustrates a robust performance towards capturing the wet pond elevations. As for UAV-photogrammetry, aside from the artefacts due to poor image overlapping adjacent to pond boundaries, void cells were spotted nearby the canopy regions. This was due to the shaded areas covered by canopies in Pond 2 (also Ponds 4 and 6 in Supplementary Figure D), where insufficient illumination was provided to expose those detailed features properly. However, these void cells tend to be marginal due to the high overlapping rate for canopy areas. This is because of a high image overlap, which improves the redundancy of point identifications, while reducing the noise and void cells in the datasets significantly.

Figure 4 shows DEM comparison between the UAV-photogrammetry and airborne-LiDAR with ground RTK-GNSS as the benchmark. Due to the inclusion of the surface vegetation from the UAV, the comparisons show overestimation of >0.5 m in the UAV-photogrammetry DEMs. In contrast, the airborne-LiDAR – which retrieves the ground reflections from the last returns – delivers more precise measurements closer to RTK-GNSS. However, such offsets scale over vegetation status thus being insignificant for Ponds 2 and 5 (also Pond 4 in Supplementary Figure D). For these cases, the discrepancies between airborne-LiDAR and UAV-photogrammetry tend to be minor according to the corresponding boxplots. Notably, underestimations of <−0.05 m were identified to the southern boundary of Pond 5 (as well as to the northern boundary of Pond 3 in Supplementary Figure D) for the airborne-LiDAR. Since airborne-LiDAR DEMs were obtained from 2015, such deviations most likely indicate a long-term sedimentation process, particularly for the low-lying locations.

3.2. Stage-curve comparisons

Figure 5 describes the comparison results of stage-curves. To intuitively understand their discrepancies, we identified the cross-section profiles from three DEMs. Here, two cross-section profiles were selected, where cross-section A is in the longest-distance directions, cross-section B is perpendicular to A (see Supplementary Figure E) and a 2 cm interval distance was used to sample the elevations. For dry Pond 5, UAV-photogrammetry demonstrates near-identical deviations of 69.51 m^2 from RTK-GNSS in comparison with 72.46 m^2 of airborne-LiDAR. Such a result is because Pond 5 only contains low vegetation, as it is regularly maintained by the municipality. Yet, in accordance with DEM comparison results, UAV-photogrammetry cross-sections illustrate overpredicted elevations in the presence of the canopy for dry Ponds 1 and 3 (see Supplementary Figure E). Accordingly, their stage-curves shift rightwards, which illustrates underestimated areas belonging to the same water levels due to such vegetation-occupied capacities. In contrast, the airborne-LiDAR obtains higher accuracies in lower RMSEs concerning the areal estimations for dry ponds. For wet Pond 2 (also Pond 4 in Supplementary Figure E), UAV-photogrammetry provides underwater elevation estimations, which demonstrates good alignment with the ground RTK-GNSS especially for shallow submerged regions. In contrast, airborne-LiDAR profiles illustrate highly elevated constant water levels of approximately 0.25–0.5 m higher than the RTK-GNSS. Without having laser returns from moisture regions (i.e., surface water, aquatic vegetations and saturated soils), airborne-LiDAR most likely overestimates the constant water levels considerably when using the 'water-edge' elevation method. Correspondingly, airborne-LiDAR stage-curves reproduce horizontal lines with none-area at the given lower water levels, which results in substantial underestimations. At this point, UAV-photogrammetry performs higher accuracies compared to airborne-LiDAR regarding RMSEs.

3.3. Outflow discharge comparison

Figure 6 illustrates the SWMM simulation results when applying three stage-area curves corresponding to Ponds 2 and 5. Figure 6(a) displays their catchment rainfall-runoff processes under the 5-year return period box rainfall. With fast catchment responses, runoff discharges (0.0025–0.18 m^3/s) were derived as the inflow, which illustrates fill-up level ratios of approximately 100% for all stormwater ponds in Supplementary Figure F. Table 3 shows a summary of the comparison results. Due to the low vegetation of <0.1 m in Pond 5, the Pond 5 demonstrates a 'goodness-of-fit' of 0.99 NSE$_{outflow}$ in hydraulic simulations when compared to RTK-GNSS, as well as airborne-LiDAR. In contrast, for Ponds 1 and 3 in Supplementary Figure F, UAV-photogrammetry obtained maximum depth difference of 0.346 and 0.293 m deviation from RTK-GNSS. Corresponding to such increased water heads (depths), differences of 0.438 and 0.434 L/s in the peak flow
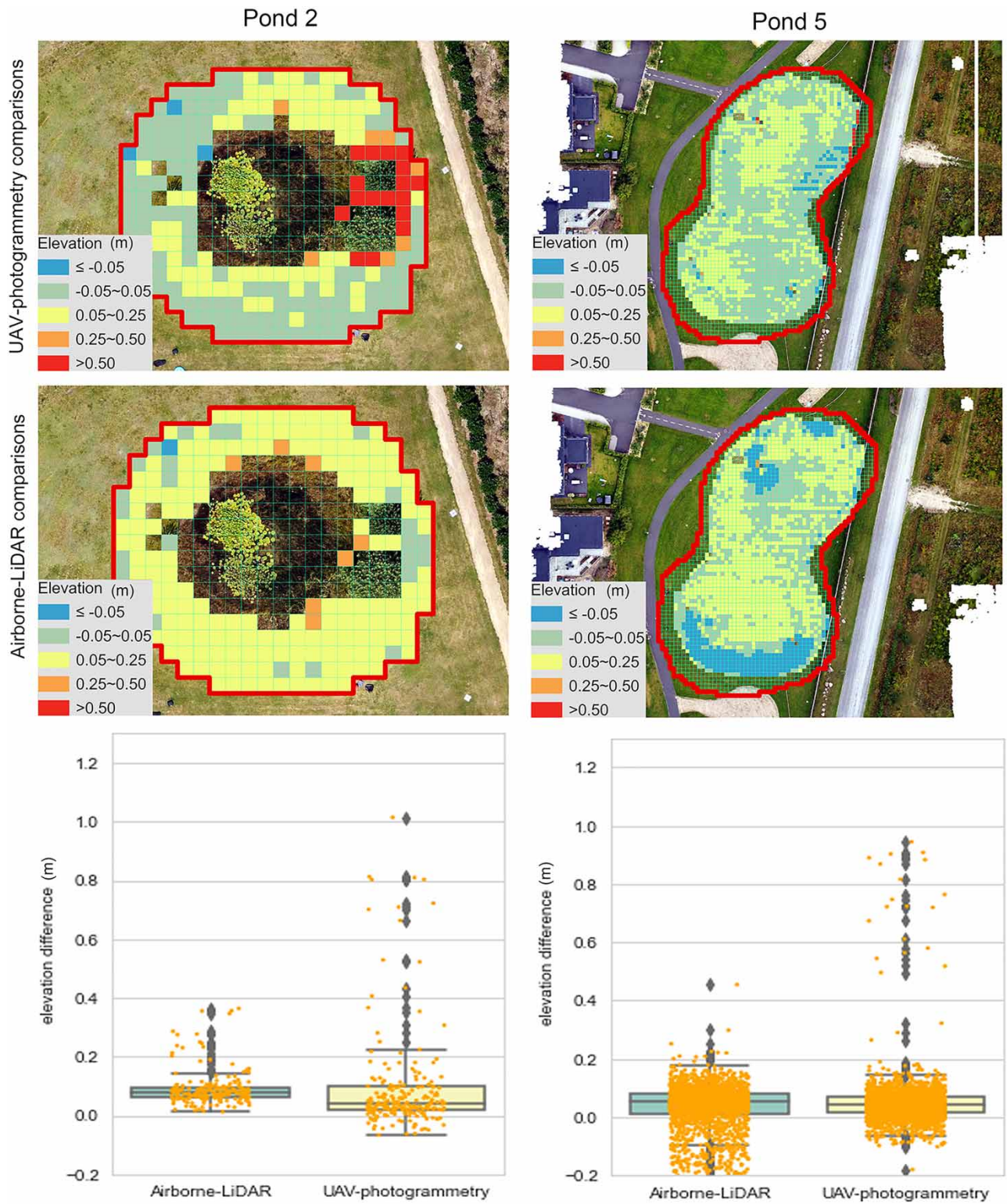
Figure 4 | Pixel-by-pixel DEM difference comparisons for Ponds 2 and 5, where boxplots represent the distribution of the elevation discrepancies against ground RTK-GNSS observations.
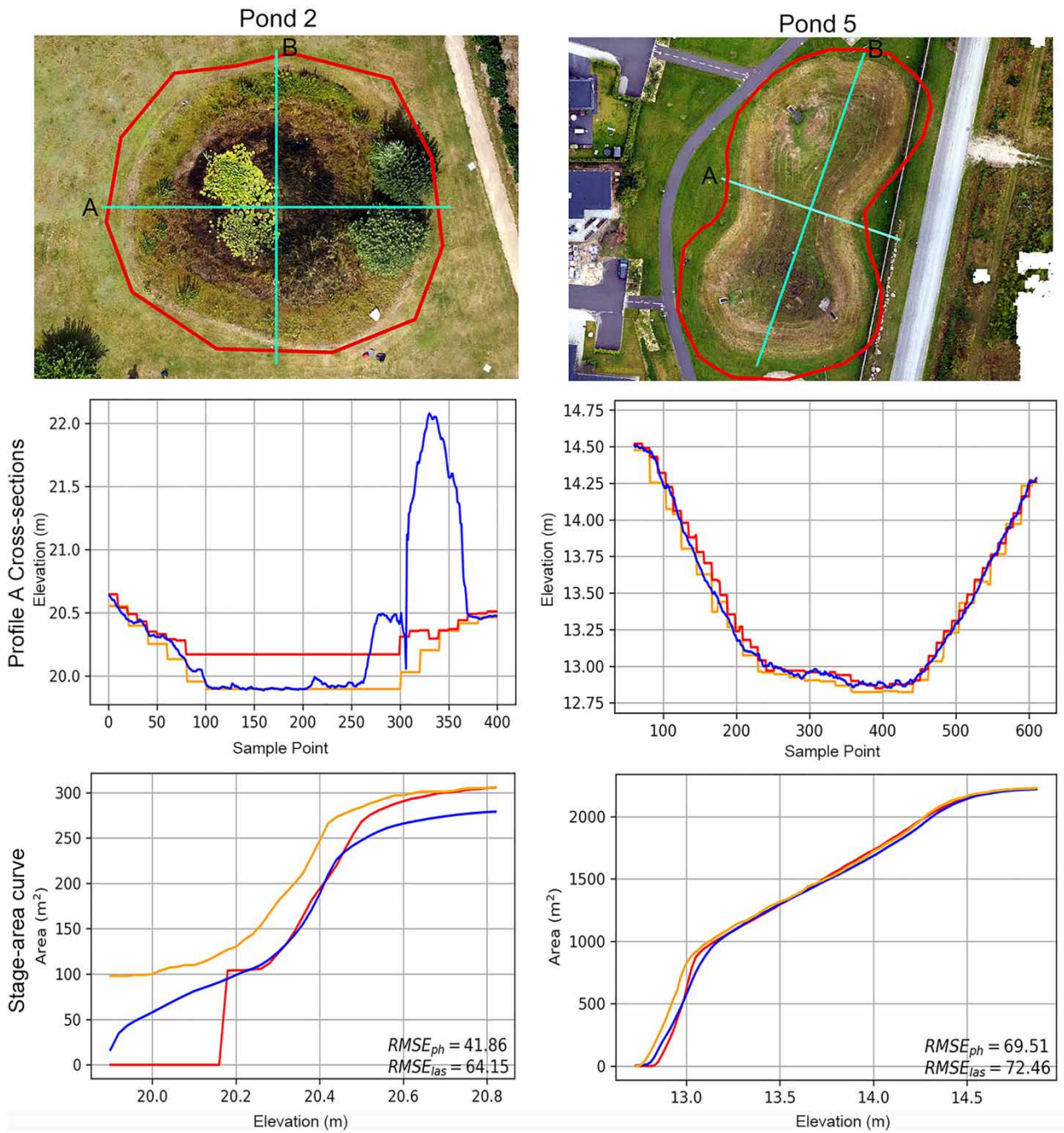
Figure 5 | Cross-section's locations and profiles; stage-curve comparisons. *Note:* Yellow lines represent RTK-GNSS, blue lines represent UAV-photogrammetry and red lines represent airborne-LiDAR. Please refer to the online version of this paper to see this figure in colour: https://dx.doi.org/10.2166/hydro.2023.178.

discharges were seen coming with a shorter empty time. Similar to stage-curve discrepancies, such hydraulic deviations are caused by the raised bottom elevations (i.e., vegetation top elevation), where the occupied vegetation volumes push the water volume upwards, resulting in the increased water heads (i.e., water depth) as well as increased outflow discharges. However, with average vegetation height deviations of 0.3–0.4 m for Ponds 1 and 3, we consider that the discrepancies indicated by $NSE_{outflow}$ of 0.88–0.89 are minor, which illustrates acceptable accuracies. For wet Pond 2 (also Pond 4 in Supplementary Figure F), discrepancies in terms of water depths and orifice discharges were observed when using airborne-LiDAR. This
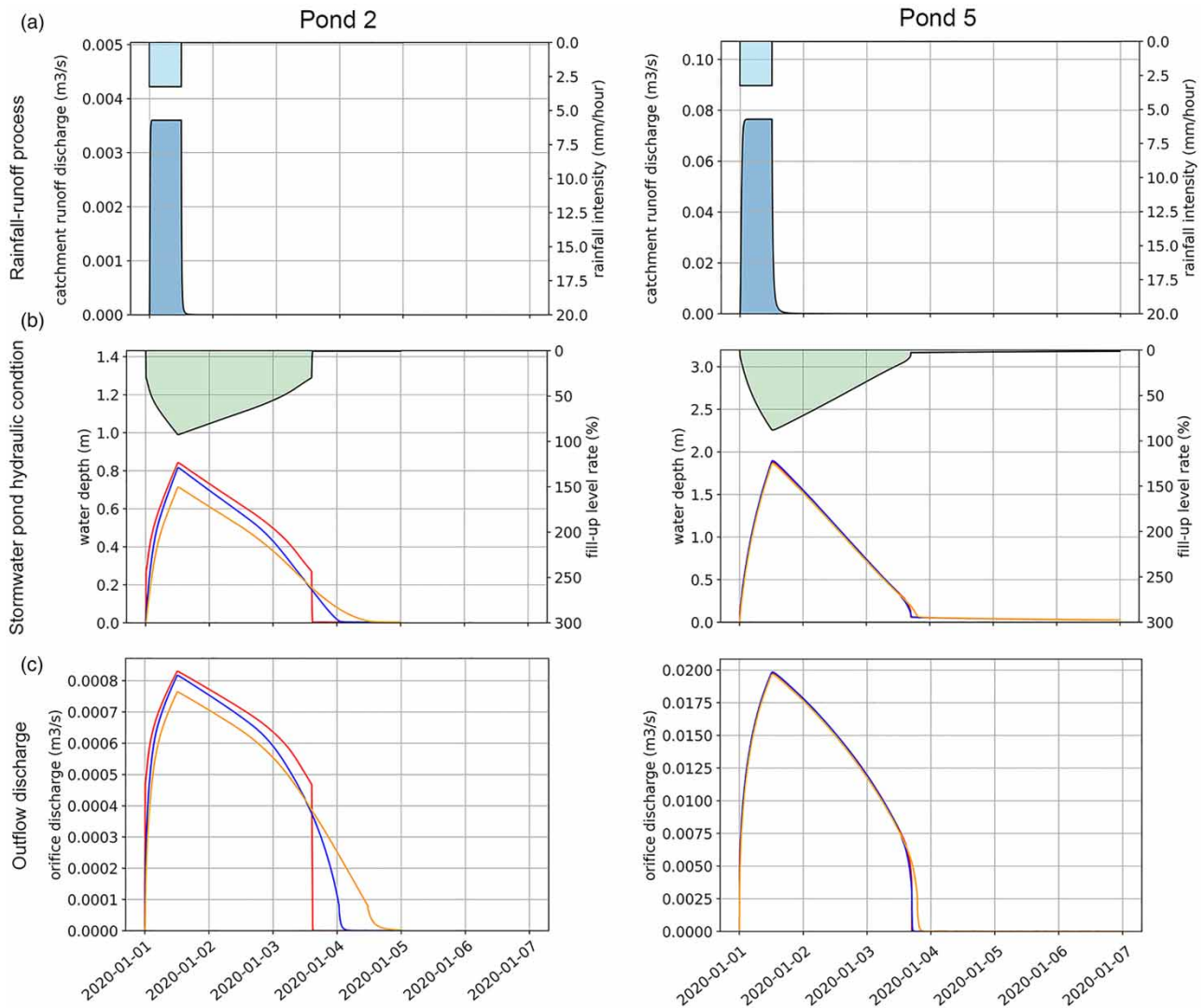
Figure 6 | (a) Rainfall-runoff process, where the light blue curve represents the box rainfall, and the dark blue curves represent the catchment runoff discharges (stormwater pond inflows) generated from synthetic urban catchments; (b) stormwater pond hydraulic conditions, where lower curves represent the water depth variations in stormwater ponds, while the light green area represents the fill-up ratio of the stormwater ponds; (c) outflow discharges, where curves stand for the orifice discharges. *Note:* Yellow lines represent RTK-GNSS, blue lines represent UAV-photogrammetry and red lines represent airborne-LiDAR. Please refer to the online version of this paper to see this figure in colour: https://dx.doi.org/10.2166/hydro.2023.178.

Table 3 | SWMM hydraulic simulation results based on UAV-photogrammetry and airborne-LiDAR in comparison against ground RTK-GNSS in terms of orifice discharges and stormwater pond water depths

Pond ID	NSE_outflow		RMSE_depth (m)		Peak flow difference (L/s)		Max depth difference (m)	
	Airborne-LiDAR	UAV-photogrammetry	Airborne-LiDAR	UAV-photogrammetry	Airborne-LiDAR	UAV-photogrammetry	Airborne-LiDAR	UAV-photogrammetry
1	0.98	0.88	0.062	0.217	0.096	0.438	0.073	0.346
2	0.54	0.87	0.117	0.071	0.061	0.054	0.127	0.112
3	0.99	0.89	0.049	0.245	0.073	0.434	0.048	0.293
4	0.15	0.70	0.114	0.089	0.072	0.080	0.132	0.145
5	0.99	0.99	0.024	0.028	0.106	0.190	0.020	0.036
6	0.78	0.98	0.023	0.108	1.951	1.282	0.283	0.183

is ascribed to the elevated bottom elevations from moisture regions presenting occupied bottom volumes, thereby resulting in hydraulic overestimations. Notably, as opposed to UAV-photogrammetry, such moisture interferences lead to significantly poor fits in 0.54 $NSE_{outflow}$ for Pond 2 (also 0.15 $NSE_{outflow}$ for Pond 4), which is unacceptable. Therefore, airborne-LiDAR is considered not suitable for wet stormwater ponds.

To mitigate vegetation impacts when implementing UAV-photogrammetry, two solutions are proposed: (i) grass removal approach, where grasses are removed physically before conducting UAV-photogrammetry or ii) shifted stage-curves approach, where stage-curves with grasses are shifted parallelly towards the direction of minimizing interception differences (i.e., vegetation height offsets from ground elevations). Here, Pond 3 – which represents medium vegetation status – was selected to test these two approaches. Figure 7 illustrates the geometric and hydraulic comparison study between before-grass removals and after-grass removals. The results demonstrate considerable improvements in the quality of DEMs after the grass removal. Without having vegetation visual blocks, the void cells due to the shaded canopy were reduced substantially in UAV-photogrammetry. Also, the hydraulic structures (i.e., inlet/outlet) were more visually distinguishable from DEMs, as well as from orthomosaic images. The stage-curves after grass removal presents goodness-of-fits against the RTK-GNSS observations, where vegetation height offsets were eliminated significantly compared to the one with grass. Moreover, the hydraulic deviations corresponding to vegetation side-effects were eliminated, where hydrographs (i.e., orifice discharges and water depths) indicate good fits against RTK-GNSS. Notably, the shifted stage-curve approach also demonstrated good alignment with the benchmarks delivering competitive accuracies regarding the grass removal approach.

4. DISCUSSION

The presented remote sensing technologies including UAV-photogrammetry and airborne-LiDAR demonstrate strong competencies in determining pond geometrics as well as hydraulics across selected stormwater ponds. Their strengths, weakness and associated potentials are discussed below in the context of dry ponds, wet ponds and general comparison.

4.1. Dry ponds comparison

According to the comparison results for dry Ponds 1, 3 and 5, it is evident that the airborne-LiDAR delivers superior performance in obtaining the ground elevations as compared to UAV-photogrammetry over vegetated terrains. This finding is in accordance with most existing literature (Gil *et al.* 2013; Jayathunga *et al.* 2018; Moudrý *et al.* 2019). Due to its poor canopy penetration capacity, the ground visibility of the UAV-photogrammetry can be reduced by the vegetation complexity, which results in overestimated elevations of 0.2–0.4 m. Yet, such discrepancies tend to make a minor hydraulic impact of 0.88–0.89 in $NSE_{outflow}$ towards the outflow discharges. Notably, since dense vegetations can disrupt the return of the laser pulse, airborne-LiDAR is also likely to result in overestimated elevations because of the poor penetration capability towards, for example, thatch layer and willows (0.15–0.26 m, Töyrä *et al.* 2003), low shrubs (0.52 m, Hopkinson *et al.* 2005), hummocks and bogs in peatland ecosystems (Luscombe *et al.* 2015; Kalacska *et al.* 2021). Similarly, UAV-LiDAR likely overestimated 0–0.3 m for short grass, >0.3 m for tall grass, 0–1 m for short shrubs and >1 m for tall shrubs (Kucharczyk *et al.* 2018). In this sense, RTK-GNSS in fact retrieves the most accurate *in-situ* ground elevation measurements compared to these two approaches. To mitigate vegetation height deviations, regardless of geometric and hydraulic aspects, the grass removal approach improved the performance of the UAV-photogrammetry significantly, obtaining RTK-GNSS comparable accuracy. In addition, it is notable that the shifted stage-curve approach suggested good alignment with RTK-GNSS, simply by offsetting the grass stage-curve with a constant height (e.g., 0.4 m). This is not the first implementation of such a method. According to Laronne & Wilhelm (2001), the shifted stage-curve approach was applied for adapting the sedimentation processes within the reservoir thus avoiding the substantial topographic remapping costs. In this case, we assume that Pond 3 was uniformly distributed with a constant vegetation height – albeit deviating from the reality – that yielded sufficient corrections in the outflow predictions. For more complicated spatial-varying vegetation structures, we recommend developing a regional offset-correction approach depending on UAV imagery. Firstly, such GIS-procedure may automatically conduct segmentations based on vegetation species observed from aerial imagery. Then the corresponding height offset ranges for each segment might be predicted from a deep learn data-driven model which learns the correlation between image pixels, vegetation species and height offset sampled from either RTK-GNSS or airborne-LiDAR datasets. Finally, proper height offsets may be adopted to each regional segments for corrections. Compared to the grass removal approach, the shifted stage-curve approach is considered an easy-fix solution with considerable advantages over large-scale surveys. Furthermore, as reported by Moudrý *et al.* (2019), UAV-photogrammetry conducted from leaf-off conditions can improve the
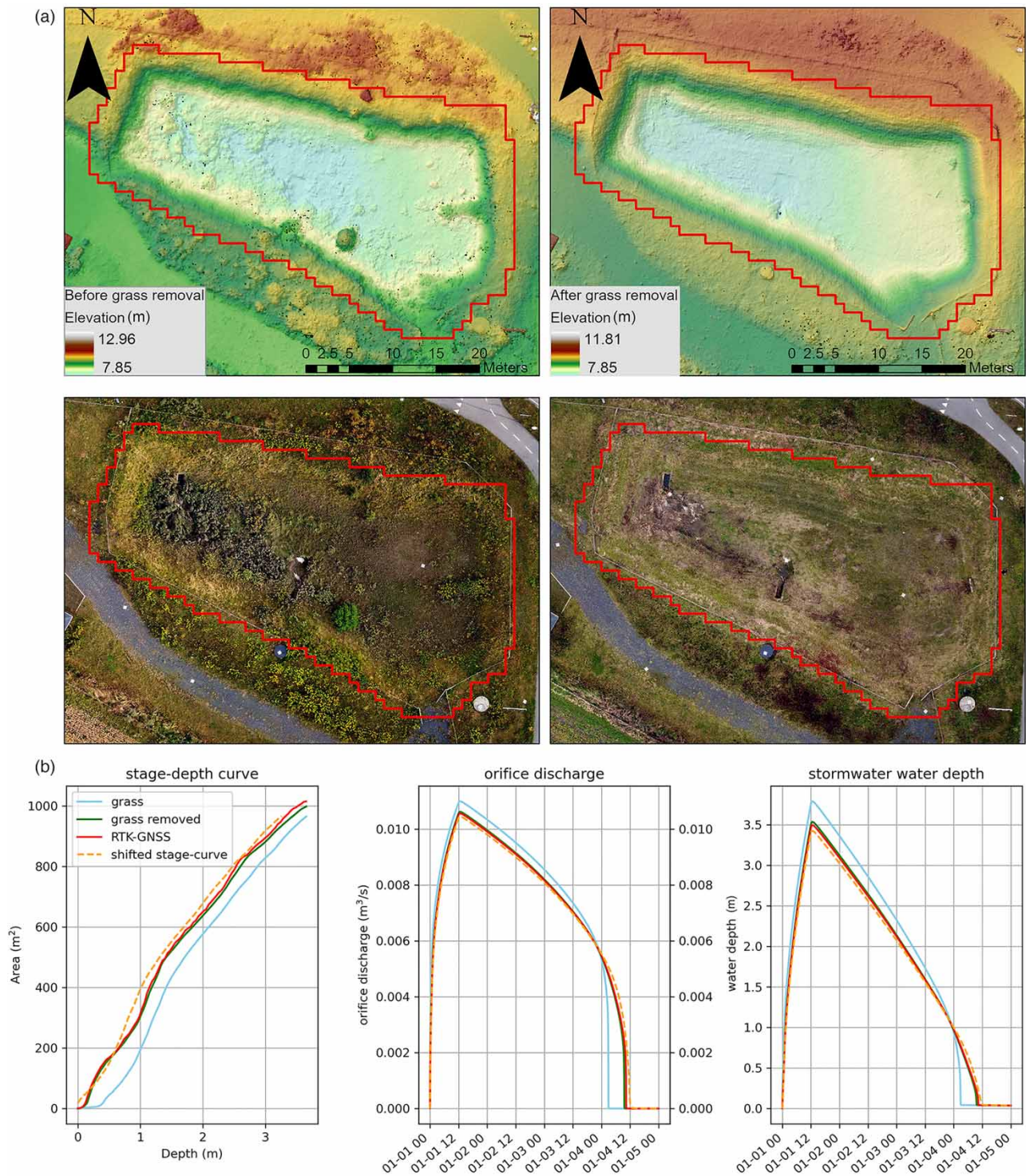
Figure 7 | (a) DEMs and orthomosaic images comparisons of Pond 3 between before grass removal and after grass removal using UAV-photogrammetry; (b) stage-curves, orifice discharges and stormwater pond water depth comparisons. *Note:* black pixels represent void cells.

bare-soil detection percentages and reduce the void cells significantly, as compared to the one from leaf-on conditions, where its DEM accuracies (at 1 m resolution) were comparable to the LiDAR-derived DTM with RMSE of 0.12–0.19 m. As such, UAV flight under leaf-off conditions were recognized as preferable options for UAV-photogrammetry survey, where time constrains are not prior considerations.

4.2. Wet ponds comparisons

According to the comparison results for wet Ponds 2, 4 and 6, UAV-photogrammetry outperforms airborne-LiDAR with respect to geometric detections as well as hydraulic simulations. This is mainly due to the moisture regions persisting in wet environments, including surface water, aquatic vegetations and saturated soils. Since most LiDAR systems operate in the infrared regions, LiDAR detection is particularly problematic for surface water detections (e.g., 10–35% returns at the flight altitude of 6 m, Huang *et al.* 2018) because of the weak laser backscatter after water absorption (Moudrý *et al.* 2019). Also, aquatic vegetations and saturated soils can dampen the returning signals, thus resulting in errors ranging from 0.14 to 0.42 m (Hopkinson *et al.* 2005; Luo *et al.* 2015; Lovitt *et al.* 2017; Moudrý *et al.* 2019), which is in accordance with our results of 0.25–0.5 m. Since aquatic vegetation stands most likely persist in wet ponds and soil, nearby surface water might be constantly saturated. UAV-photogrammetry employing a passive sensor does not encounter such issues, and is therefore considered more robust in moist environments compared to LiDAR. Hydraulically, such discrepancies derived from LiDAR lead to poor fits with $NSE_{outflow}$ of 0.15–0.54, which is unacceptable.

Interestingly, the through-water photogrammetry retrieved underwater elevations for the wet ponds in our study. Based on existing literatures, through-water photogrammetry has been extensively implemented in the collection of bathymetric data for the riverine and stream environment (Bagheri *et al.* 2015; Tamminga *et al.* 2015b; Woodget *et al.* 2015; Dietrich 2017; Shintani & Fonstad 2017; Bandini *et al.* 2018). However, UAV-photogrammetry tends to over-predict elevations in submerged zones due to the refraction of light at the air–water interface. With <0.7 m shallow clear water in adequate illumination conditions, the UAV-photogrammetry approach following refraction correction reproduces good underwater estimations, with errors of 0.004–0.06 m compared to the bathymetric laser scanning (Woodget *et al.* 2015). According to Westaway *et al.* (2000), in instances of water depths shallower than 0.2 m, such effects of refraction are negligible. Notably, instead of existing water volumes under water surfaces, we are interested in available flood detention capacities that are excess volumes above the constant water levels. In this sense, bathymetric data acquired by through-water photogrammetry within the submerged zones might not be of particular interest in the context of urban flood prevention. Nevertheless, the interferences between a pond's standing water and its shallow groundwater tables might correspond significantly to seasonal variations. According to Danish national groundwater predictions from 'DK-Model HIP' (SDFE 2021a, 2021b), the seasonal groundwater depth differences between winter and summer for Ponds 2 and 4 reach 0.12–0.165 m. Here, we believe that a buffer of 0.2 m depth bathymetric detection ranges from the through-water photogrammetry would address these seasonal uncertainties sufficiently. Notably, the bathymetric LiDAR operating at the green wavelength of 532 nm can penetrate water columns with less attenuation than infrared-LiDAR and thus measuring the underwater topography in a high accuracy (Szafarczyk & Toś 2023). Yet, such bathymetric scanner requires the simultaneous use of two lasers (i.e., infrared and green) thus demanding a dual-channel hybrid LiDAR system (e.g., RIEGL VQ-1560), which boosts the cost significantly. Again, accounting for the specific application context in this study, we think such a trade-off between a 'good-to-have' accuracy and the substantially increased economic costs does not sound like wise option particularly considering the limited budget scenario. Aside from this, the central aquatic vegetations floating above the water surface of Pond 4 block the visibility of underwater features, thus resulting in overpredicted bottom elevations (Supplementary Figure E). However, these floating features also construct a stable visual point of the water surface elevations for UAV-photogrammetry, thus extending its application towards surface water elevation detections. In this instance, we think that UAV-photogrammetry along with floating artificial objects can provide – at least for the static water surface in wet ponds – more cost-efficient solutions compared to the radar altimetry reported by Bandini *et al.* (2020).

4.3. General comparison

The space-borne and air-borne remote sensing technologies have shown excellent performance in past decades regarding many hydrological applications (i.e., soil moisture, large surface water body, snow and glacier) at basin-scale or even up to a continent scale (Pietroniro & Leconte 2005). Nevertheless, in the sense of the local urban catchment scale and urban water management applications, we consider UAV-photogrammetry is a more competitive option to the two alternatives particularly in obtaining high-resolution datasets. In this study, UAV-photogrammetry presents a hyperspatial remote sensing solution delivering highly densified 3D point clouds corresponding to sub-centimetre DEMs (e.g., <2 cm). This allows for the intuitive reflections of substantial geometric details in stormwater ponds, such as critical hydraulic structures (i.e., inlets, outlets and weirs, details <0.1 m), which are essential in hydraulic simulations. Whereas airborne-LiDAR in our case also provides high-resolution datasets in approximate 50 cm, such resolution is still considered 'not-sharp-enough' in capturing those micro-topographies. This is ascribed to the instinct inherent in LiDAR techniques, where the laser footprint resolution limits the discrimination of the small

geometric features. Here, two consequences are illustrated: (i) miss-interpolations of the break-line features, i.e., ridges and cliff edges (Gil *et al.* 2013), where such similar edge features most likely compose man-made structures in stormwater ponds; (ii) overestimated ground elevations as the miss-reflect of the micro-topographic features, for instance small shrubs <1 m, vertical walls (Barnea & Filin 2008), short vegetations (Webster & Dias 2006) and small trees (Thiel & Schmullius 2017); thus miss-recognizing their top elevations as the bare-soil (Gil *et al.* 2013). Such discrepancies tend to be minor, at <0.2 m, which is in accordance with our findings of <0.25 m (see Supplementary Figure D). In response to such drawbacks, UAV amounted with multi-return LiDAR that conducts the LiDAR scanning at a much lower altitude could reproduce higher point cloud density up to 19.4 ± 7.5 ppm^2 (albeit sparser than 570.4 ± 172.8 ppm^2 from UAV-photogrammetry), thus delivering high-quality DEM at 0.1 m resolution, as opposed to the point density of 2–4 ppm^2 from the airborne scanning (Kalacska *et al.* 2021). However, the use of multi-return LiDAR inevitably boosts a higher payload, thereby demanding more advanced UAV platforms with additional accessories (i.e., PPK/RTK-GNSS and IMU). This results in prohibitive total costs. According to Bandini *et al.* (2020), the LiDAR system (i.e., Puck LITE™ providing dual return with a NIR) with PPK/RTK-GNSS, weighs 1 kg. Such a payload demands DJI Matrice 600 PRO to take them off, where the total costs rise to above \$15,400. In contrast, DJI Mini2 integrating 4K camera and the gimbal weighs only 249 g and costs a total of \$449 (DJI, China 2021), whereby substantial economic advantages are illustrated when compared to either UAV-LiDAR or airborne-LiDAR. In addition, this lightweight aircraft of <250 g encounters the least resistance in the aircraft regulations (i.e., no registrations and no certificates) globally (e.g., China, US and EU 2021), thereby requiring fewer extra works from the non-specialist. Moreover, the foldable, pocket-size UAV platform is more portable for engineering field work compared to the big ones. The system integrates hardware and software all in one system, which is more user-friendly for the less-experienced drone pilots. As such, we consider such Mini-UAV-based photogrammetry options to be an economical solution and thus suitable for low-budget research, as well as water engineering practices in third-world countries.

Shortcomings and the associated potentials that persist for UAV-photogrammetry can be summarized as four aspects. First of all, according to Hopkinson *et al.* (2009), insufficient illuminations might introduce bias, particularly for shaded areas. In line with Leitão *et al.* (2016), we experienced few discrepancies in UAV-photogrammetry datasets regardless of weather conditions (i.e., sunny days or overcast days). This might be ascribed to either the relatively simple/regular topography constructed in stormwater ponds or robustness of the algorithm adopted in the SfM software. Yet, if any such problem occurs, we think a potential solution could be to compensate image exposures by having multiple camera views, covering the pond from multiple angles in different flight altitudes. Secondly, SfM processing time tends to be significantly more expensive than LiDAR, particularly when including many aerial images. Here, we suggest that a target-based optimization algorithm might be a feasible solution (Zhao *et al.* 2021). To identify the minimized computational costs, such a procedure would cover target objects (i.e., stormwater ponds) while maintaining high overlapping rates with minimum pre-selected critical aerial images, as well as optimized spatial configuration in footprints. Thirdly, we used Ground RTK-GNSS to collect 15 GCPs, which adds an extra 10–20 min. Instead, direct georeferencing technologies can be adopted to avoid GCPs (Cramer *et al.* 2000; Rehak *et al.* 2013; Turner *et al.* 2013; Carbonneau & Dietrich 2017). Yet, for the case of DJI Mini2, a PPK Upgrade Kit that consists of a PPK-GNSS along with built-in IMU is required to deliver a highly accurate self-positioning (TOPODRONE 2021), which certainly adds extra cost. Last but not least, as opposed to the one-strip aerial scanning via LiDAR, the UAV-photogrammetry must conduct multi-strip flights in order to obtain a high degree of overlapping within observed regions of interest. When upscaling to the national scale survey, UAV-photogrammetry might not be the most efficient remote sensing option, particularly considering the available maximum flight time (e.g., 31 min for DJI Mini2). Based hereon, the UAV-photogrammetry is more suitable for the small case area (Kalacska *et al.* 2021). Yet, airborne-LiDAR costs significantly more compared to UAV-photogrammetry, thus leading to lower observation update frequency (e.g., 5 years) which likely results in out-of-date observations. For the instance of Pond 6, due to post-constructions, DEM discrepancies of 0.2–0.4 m were obtained when using airborne-LiDAR (see Supplementary Figure D). Hydraulically, such post-construction errors present higher deviations (i.e., NSE$_{outflow}$ of 0.78) when comparing to vegetation errors (i.e., NSE$_{outflow}$ of 0.88), but less than LiDAR laser pulse miss-reflection errors (i.e., NSE$_{outflow}$ of 0.15–0.54). As such, we think UAV-photogrammetry which provides up-to-date and detailed observations for small cases can provide a complementary solution alternative to airborne-LiDAR. Furthermore, according to our experiences, UAV-photogrammetry takes flight time less than 5–10 min to accomplish multi-strips scanning delivering high-quality DEM. As opposed to the conventional topographic survey using the total stations or the ground RTK-GNSS, which tends to be labor-intensive (e.g., 3–14 workdays to authors' experience for each pond) and likely involving human-related systematic bias, UAV-photogrammetry improves the survey efficiency

considerably. Accounting for several times lower costs for such lightweight UAVs than LiDAR options, we would further highlight the potential for implementing multi-UAV collaborative photogrammetry survey, which could address all above-mentioned limitations (Pajares 2015). Here, a UAVs fleet collaborates on a common photogrammetry survey task by having data transmission or image sharing from a blackboard communication system. With broader spatial coverages, more efficient image overlapping based on multi-UAV coordination and minimized blind spot via multiple camera views from different flight altitudes/angles, this approach would reduce the data redundancy considerably and further enhance the survey efficiency of the UAV-photogrammetry towards multiple ponds at a large scale (Jensen *et al.* 2009).

5. CONCLUSIONS

This paper investigates and compares the two remote sensing technologies (i.e., UAV-photogrammetry and airborne-LiDAR) for stormwater pond geometric detections, as well as the corresponding outflow discharge determinations in the context of the urban stormwater management. Six stormwater ponds of various sizes, types, vegetation statuses, topographic complications and catchment characteristics were chosen as the test cases. Benchmarked against the ground-truth *in-situ* observations from RTK-GNSS, UAV-photogrammetry was compared with airborne-LiDAR on three levels: (i) DEMs, (ii) stage-curves and (iii) outflow discharges, where the validation sequence corresponded to the actual data processing workflow. Furthermore, their strengths, weakness and associated potentials were discussed from three aspects: (i) dry ponds, (ii) wet ponds and (iii) general applications. The main findings are outlined as follows:

- For dry ponds, UAV-photogrammetry illustrates overestimations of 0.2–0.4 m in DEMs for the sake of its poor penetration capacity towards vegetation, indicating higher deviations compared to airborne-LiDAR. Yet, from a hydraulic perspective, such discrepancies lead to insignificant impact (i.e., $NSE_{outflow}$ of 0.88–0.89) towards the outflow discharges. To improve this issue, a grass removal approach demonstrates a good fit for the benchmarks, and is thus considered a feasible solution. In addition, the shifted stage-curve approach that results in acceptable accuracy is recognized as an easy correction method to mitigate the vegetation hydraulic side-effect for large-scale survey cases.

- For wet ponds, UAV-photogrammetry outperforms the airborne-LiDAR (i.e., infrared beam operated at 1,550 nm wavelength) in terms of both geometric detections and outflow discharges. Since surface water, aquatic vegetation and saturated soils can dampen the returning of laser signals, the airborne-LiDAR yields higher bottom elevations of 0.25–0.5 m than RTK-GNSS. Such discrepancies result in $NSE_{outflow}$ of 0.15–0.54, which is unacceptable. Here, we conclude that the airborne-LiDAR with the infrared beam sensor is not suitable for wet ponds. In contrast, UAV-photogrammetry provides underwater estimations via the through-water photogrammetry, and therefore illustrates robust performance towards moisture environments, as well as seasonal variations in groundwater. Furthermore, UAV-photogrammetry, along with floating artificial objects, would extend its application for surface water elevation detection – at least for static water.

- UAV-photogrammetry presents a hyperspatial remote sensing capability superior to airborne-LiDAR, thus delivering high-quality DEMs <2 cm resolution. Such sharp resolution provides a better outlining of the break-line features inherent in man-made hydraulic structures than LiDAR, for instance inlets, outlets and weirs. Besides, lightweight UAVs demonstrate substantial economic advantages over either airborne-LiDAR or UAV-LiDAR options. Thus, it is recommended as the preferred option for low-budget research, as well as water engineering practice for third-world countries.

- Shortcomings persist for UAV-photogrammetry. First of all, it tends to yield high void fraction in conditions of insufficient illumination. Secondly, the process time of SfM can be substantially more expensive, particularly when including many images. Thirdly, its indirect georeferencing costs extra time, and adding a direct georeferencing module would inevitably increase costs. Finally, in contrast to the LiDAR's one-strip aerial scanning, multi-strip aerial scanning must be carried out in UAV-photogrammetry to obtain a high overlapping rate, which results in a slightly longer flight time (i.e., 5–10 min) compared to LiDAR. Nevertheless, the multi-UAVs collaborative photogrammetry survey was highlighted to address all these challenges and would further extend its application towards large-scale surveys.

DATA AVAILABILITY STATEMENT

Data cannot be made publicly available; readers should contact the corresponding author for details.

CONFLICT OF INTEREST

The authors declare there is no conflict.

REFERENCES

Agisoft Metashape User Manual 2021. Available from: https://www.agisoft.com/pdf/metashape-pro_1_7_en.pdf.

Agüera-Vega, F., Carvajal-Ramírez, F. & Martínez-Carricondo, P. 2017a Accuracy of digital surface models and orthophotos derived from unmanned aerial vehicle photogrammetry. *Journal of Surveying Engineering* **143** (2), 04016025.

Agüera-Vega, F., Carvajal-Ramírez, F. & Martínez-Carricondo, P. 2017b Assessment of photogrammetric mapping accuracy based on variation ground control points number using unmanned aerial vehicle. *Measurement* **98**, 221–227.

Arnold, E. & Toran, L. 2018 Effects of bank vegetation and incision on erosion rates in an urban stream. *Water* **10** (4), 482.

Bagheri, O., Ghodsian, M. & Saadatseresht, M. 2015 Reach scale application of UAV+ SfM method in shallow rivers hyperspatial bathymetry. *The International Archives of Photogrammetry, Remote Sensing and Spatial Information Sciences* **40** (1), 77.

Balstrøm, T. & Crawford, D. 2018 Arc-Malstrøm: A 1D hydrologic screening method for stormwater assessments based on geometric networks. *Computers & Geosciences* **116**, 64–73.

Bandini, F., Olesen, D., Jakobsen, J., Kittel, C. M. M., Wang, S., Garcia, M. & Bauer-Gottwein, P. 2018 Bathymetry observations of inland water bodies using a tethered single-beam sonar controlled by an unmanned aerial vehicle. *Hydrology and Earth System Sciences* **22** (8), 4165–4181.

Bandini, F., Sunding, T. P., Linde, J., Smith, O., Jensen, I. K., Köppl, C. J., Butts, M. & Bauer-Gottwein, P. 2020 Unmanned aerial system (UAS) observations of water surface elevation in a small stream: Comparison of radar altimetry, LIDAR and photogrammetry techniques. *Remote Sensing of Environment* **237**, 111487.

Barnea, S. & Filin, S. 2008 Keypoint based autonomous registration of terrestrial laser point-clouds. *ISPRS Journal of Photogrammetry and Remote Sensing* **63**, 19–35. doi:10.1016/j.isprsjprs.2007.05.005.

Carbonneau, P. E. & Dietrich, J. T. 2017 Cost-effective non-metric photogrammetry from consumer-grade sUAS: Implications for direct georeferencing of structure from motion photogrammetry. *Earth Surface Processes and Landforms* **42** (3), 473–486.

Chen, Q., Cheng, H., Yang, Y., Liu, G. & Liu, L. 2014 Quantification of mass wasting volume associated with the giant landslide Daguangbao induced by the 2008 Wenchuan earthquake from persistent scatterer InSAR. *Remote Sensing of Environment* **152**, 125–135.

Chou, T.-Y., Yeh, M.-L., Chen, Y. C. & Chen, Y. H. 2010 Disaster monitoring and management by the unmanned aerial vehicle technology.

Cramer, M., Stallmann, D. & Haala, N. 2000 Direct georeferencing using GPS/inertial exterior orientations for photogrammetric applications. *International Archives of Photogrammetry and Remote Sensing* **33** (B3/1; PART 3), 198–205.

Danish Basic Data Program 2021 Available from: https://ec.europa.eu/cefdigital/wiki/display/CEFDIGITAL/2019/07/25/Danish+Basic+Data+Program.

Dietrich, J. T. 2017 Bathymetric structure-from-motion: Extracting shallow stream bathymetry from multi-view stereo photogrammetry. *Earth Surface Processes and Landforms* **42** (2), 355–364.

DJI, China 2021 Available from: https://www.dji.com/dk/mini-2?site=brandsite&from=homepage.

Dominici, D., Baiocchi, V., Zavino, A., Alicandro, M. & Elaiopoulos, M. 2012 Micro UAV for post seismic hazards surveying in old city center of L'Aquila. In *Paper Presented at the Proceedings of the FIG Working Week*.

Eltner, A., Baumgart, P., Maas, H. G. & Faust, D. 2015 Multi-temporal UAV data for automatic measurement of rill and interrill erosion on loess soil. *Earth Surface Processes and Landforms* **40** (6), 741–755.

Emerson, C. H., Welty, C. & Traver, R. G. 2005 Watershed-scale evaluation of a system of storm water detention basins. *Journal of Hydrologic Engineering* **10** (3), 237–242.

Feng, Q., Liu, J. & Gong, J. 2015 Urban flood mapping based on unmanned aerial vehicle remote sensing and random forest classifier – A case of Yuyao, China. *Water* **7** (4), 1437–1455.

Flener, C., Vaaja, M., Jaakkola, A., Krooks, A., Kaartinen, H., Kukko, A., Kasvi, E., Hyyppa, H., Hyyppa, J. & Alho, P. 2013 Seamless mapping of river channels at high resolution using mobile LiDAR and UAV-photography. *Remote Sensing* **5** (12), 6382–6407.

Gebrehiwot, A. & Hashemi-Beni, L. 2020 Automated indunation mapping: Comparison of methods. In *Paper Presented at the IGARSS 2020-2020 IEEE International Geoscience and Remote Sensing Symposium*.

Gebrehiwot, A. A. & Hashemi-Beni, L. 2021 Three-dimensional inundation mapping using UAV image segmentation and digital surface model. *ISPRS International Journal of Geo-Information* **10** (3), 144.

Geipel, J., Link, J. & Claupein, W. 2014 Combined spectral and spatial modeling of corn yield based on aerial images and crop surface models acquired with an unmanned aircraft system. *Remote Sensing* **6** (11), 10335–10355.

Gil, A. L., Núñez-Casillas, L., Isenburg, M., Benito, A. A., Bello, J. J. R. & Arbelo, M. 2013 A comparison between LiDAR and photogrammetry digital terrain models in a forest area on Tenerife Island. *Canadian Journal of Remote Sensing* **39** (5), 396–409.

Hopkinson, C. 2007 The influence of flying altitude, beam divergence, and pulse repetition frequency on laser pulse return intensity and canopy frequency distribution. *Canadian Journal of Remote Sensing* **33** (4), 312–324.

Hopkinson, C., Chasmer, L. E., Sass, G., Creed, I. F., Sitar, M., Kalbfleisch, W. & Treitz, P. 2005 Vegetation class dependent errors in LiDAR ground elevation and canopy height estimates in a boreal wetland environment. *Canadian Journal of Remote Sensing* **31** (2), 191–206.

Hopkinson, C., Hayashi, M. & Peddle, D. 2009 Comparing alpine watershed attributes from LiDAR, photogrammetric, and contour-based digital elevation models. *Hydrological Processes: An International Journal* **23** (3), 451–463.

Huang, Z. C., Yeh, C. Y., Tseng, K. H. & Hsu, W. Y. 2018 A UAV–RTK LiDAR system for wave and tide measurements in coastal zones. *Journal of Atmospheric and Oceanic Technology* **35** (8), 1557–1570.

Hundecha, Y. & Bárdossy, A. 2004 Modeling of the effect of land use changes on the runoff generation of a river basin through parameter regionalization of a watershed model. *Journal of Hydrology* **292** (1–4), 281–295.

Jayathunga, S., Owari, T. & Tsuyuki, S. 2018 Evaluating the performance of photogrammetric products using fixed-wing UAV imagery over a mixed conifer–broadleaf forest: Comparison with airborne laser scanning. *Remote Sensing* **10** (2), 187.

Jensen, A. M., Morgan, D., Chen, Y., Clemens, S. & Hardy, T. 2009 Using multiple open-source low-cost unmanned aerial vehicles (UAV) for 3D photogrammetry and distributed wind measurement. In: *International Design Engineering Technical Conferences and Computers and Information in Engineering Conference*, Vol. 49002, pp. 629–634.

Kääb, A. & Leprince, S. 2014 Motion detection using near-simultaneous satellite acquisitions. *Remote Sensing of Environment* **154**, 164–179.

Kalacska, M., Arroyo-Mora, J. P. & Lucanus, O. 2021 Comparing UAS LiDAR and structure-from-motion photogrammetry for peatland mapping and virtual reality (VR) visualization. *Drones* **5** (2), 36.

Karamuz, E., Romanowicz, R. J. & Doroszkiewicz, J. 2020 The use of unmanned aerial vehicles in flood hazard assessment. *Journal of Flood Risk Management* **13** (4), e12622.

Kucharczyk, M., Hugenholtz, C. H. & Zou, X. 2018 UAV–LiDAR accuracy in vegetated terrain. *Journal of Unmanned Vehicle Systems* **6** (4), 212–234.

Langhammer, J. & Vacková, T. 2018 Detection and mapping of the geomorphic effects of flooding using UAV photogrammetry. *Pure and Applied Geophysics* **175** (9), 3223–3245.

Laronne, J. B. & Wilhelm, R. 2001 Shifting stage-volume curves: predicting event sedimentation rate based on reservoir stratigraphy. In: *Applying Geomorphology to Environmental Management* (Anthony, D. J., Harvey, M. D., Laronne, J. B. & Mosley, M. P. eds.). Water Resources Publications, LLC, Highlands Ranch, CO, USA, pp. 33–54.

Leica Geosystems 2021. Available from: https://leica-geosystems.com/products/total-stations/software/leica-smartworx-viva.

Leitão, J. P., Moy de Vitry, M., Scheidegger, A. & Rieckermann, J. 2016 Assessing the quality of digital elevation models obtained from mini unmanned aerial vehicles for overland flow modelling in urban areas. *Hydrology and Earth System Sciences* **20** (4), 1637–1653.

Li, H. 2020 Investigation of highway stormwater management pond capacity for flood detention and water quality treatment retention via remote sensing data and conventional topographic survey. *Transportation Research Record* **2674** (7), 514–527.

Li, B., Hou, J., Li, D., Yang, D., Han, H., Bi, X., Wang, X., Hinkelmann, R. & Xia, J. 2021 Application of LiDAR UAV for high-resolution flood modelling. *Water Resources Management* **35** (5), 1433–1447.

Liu, H., Wang, L., Sherman, D., Gao, Y. & Wu, Q. 2010 An object-based conceptual framework and computational method for representing and analyzing coastal morphological changes. *International Journal of Geographical Information Science* **24** (7), 1015–1041.

Liu, F., Nielsen, A. H. & Vollertsen, J. 2019a Sorption and degradation potential of pharmaceuticals in sediments from a stormwater retention pond. *Water* **11** (3), 526.

Liu, F., Vianello, A. & Vollertsen, J. 2019b Retention of microplastics in sediments of urban and highway stormwater retention ponds. *Environmental Pollution* **255**, 113335.

Liu, X. 2008 Airborne LiDAR for DEM generation: Some critical issues. *Progress in Physical Geography* **32** (1), 31–49.

Lovitt, J., Rahman, M. M. & McDermid, G. J. 2017 Assessing the value of UAV photogrammetry for characterizing terrain in complex peatlands. *Remote Sensing* **9** (7), 715.

Lowe, D. G. 1999 Object recognition from local scale-invariant features. In: *Proceedings of the Seventh IEEE International Conference on Computer Vision*, Vol. 2. IEEE, pp. 1150–1157.

Luo, S., Wang, C., Pan, F., Xi, X., Li, G., Nie, S. & Xia, S. 2015 Estimation of wetland vegetation height and leaf area index using airborne laser scanning data. *Ecological Indicators* **48**, 550–559.

Luscombe, D. J., Anderson, K., Gatis, N., Wetherelt, A., Grand-Clement, E. & Brazier, R. E. 2015 What does airborne LiDAR really measure in upland ecosystems? *Ecohydrology* **8** (4), 584–594.

Mason, D. C., Horritt, M. S., Hunter, N. M. & Bates, P. D. 2007 Use of fused airborne scanning laser altimetry and digital map data for urban flood modelling. *Hydrological Processes: An International Journal* **21** (11), 1436–1447.

McDonnell, B. E., Ratliff, K., Tryby, M. E., Wu, J. J. X. & Mullapudi, A. 2020 PySWMM: The python interface to stormwater management model (SWMM). *Journal of Open Source Software* **5** (52), 2292.

Miljøstyrelsen 2019 Bekendtgørelse af lov om miljøbeskyttelse, LBK nr 681 af 02/07/2019 (in Danish).

Moudrý, V., Gdulová, K., Fogl, M., Klápště, P., Urban, R., Komárek, J., Moudrá, L., Štroner, M., Barták, V. & Solský, M. 2019 Comparison of leaf-off and leaf-on combined UAV imagery and airborne LiDAR for assessment of a post-mining site terrain and vegetation structure: Prospects for monitoring hazards and restoration success. *Applied Geography* **104**, 32–41.

Pajares, G. 2015 Overview and current status of remote sensing applications based on unmanned aerial vehicles (UAVs). *Photogrammetric Engineering & Remote Sensing* **81** (4), 281–330.

Perks, M. T., Russell, A. J. & Large, A. R. 2016 Advances in flash flood monitoring using unmanned aerial vehicles (UAVs). *Hydrology and Earth System Sciences* **20** (10), 4005–4015.

Pietroniro, A. & Leconte, R. 2005 A review of Canadian remote sensing and hydrology, 1999–2003. *Hydrological Processes: An International Journal* **19** (1), 285–301.

Rehak, M., Mabillard, R. & Skaloud, J. 2013 A micro-UAV with the capability of direct georeferencing (No. CONF, pp. 317-323). ISPRS Archives.

Rivas Casado, M., Irvine, T., Johnson, S., Palma, M. & Leinster, P. 2018 The use of unmanned aerial vehicles to estimate direct tangible losses to residential properties from flood events: A case study of Cockermouth following the Desmond storm. *Remote Sensing* **10** (10), 1548.

Rossman, L. A. 2007 *Storm Water Management Model User's Manual*. EPA/600/R-05/040, U.S. Environmental Protection Agency, Cincinnati, OH.

SDFE 2020 *Danish Agency for Data Supply and Efficiency*. Available from: https://kortforsyningen.dk/sites/default/files/dhm-prodspec-v1.0.0.pdf.

SDFE 2021a *HIP Sammenfatningsrapporten*. Available from: https://sdfe.dk/media/2920241/sammenfatningsrapport-hip4plus31jan2021.pdf.

SDFE 2021b Available from: https://eng.sdfe.dk/about-us/organisation/data-bank/.

Shintani, C. & Fonstad, M. A. 2017 Comparing remote-sensing techniques collecting bathymetric data from a gravel-bed river. *International Journal of Remote Sensing* **38** (8–10), 2883–2902.

Suriya, S. & Mudgal, B. 2012 Impact of urbanization on flooding: the Thirusoolam sub watershed – A case study. *Journal of Hydrology* **412**, 210–219.

Szafarczyk, A. & Toś, C. 2023 The use of green laser in LiDAR bathymetry: State of the Art and recent advancements. *Sensors* **23** (1), 292.

Tamminga, A. D., Eaton, B. C. & Hugenholtz, C. H. 2015a UAS-based remote sensing of fluvial change following an extreme flood event. *Earth Surface Processes and Landforms* **40** (11), 1464–1476.

Tamminga, A., Hugenholtz, C., Eaton, B. & Lapointe, M. 2015b Hyperspatial remote sensing of channel reach morphology and hydraulic fish habitat using an unmanned aerial vehicle (UAV): A first assessment in the context of river research and management. *River Research and Applications* **31** (3), 379–391.

Thiel, C. & Schmullius, C. 2017 Comparison of UAV photograph-based and airborne LiDAR-based point clouds over forest from a forestry application perspective. *International Journal of Remote Sensing* **38** (8–10), 2411–2426.

Thomsen, A. T. H. 2019 *Quantification of the Hydraulic Effects of Discharge From Stormwater Detention Ponds Into Streams*.

TOPODRONE 2021 TOPODRONE DJI Mavic Mini/Mini 2 PPK Upgrade Kit. Available from: https://topodrone.org/product/kits/pro-uk/mm-uk-ppk/.

Töyrä, J., Pietroniro, A., Hopkinson, C. & Kalbfleisch, W. 2003 Assessment of airborne scanning laser altimetry (LiDAR) in a deltaic wetland environment. *Canadian Journal of Remote Sensing* **29** (6), 718–728.

Trepekli, K., Balstrøm, T., Friborg, T., Fog, B., Allotey, A. N., Kofie, R. Y. & Møller-Jensen, L. 2022 UAV-borne, LiDAR-based elevation modelling: A method for improving local-scale urban flood risk assessment. *Natural Hazards* **113** (1), 423–451.

Tsubaki, R. & Fujita, I. 2010 Unstructured grid generation using LiDAR data for urban flood inundation modelling. *Hydrological Processes: An International Journal* **24** (11), 1404–1420.

Turner, D., Lucieer, A. & Wallace, L. 2013 Direct georeferencing of ultrahigh-resolution UAV imagery. *IEEE Transactions on Geoscience and Remote Sensing* **52** (5), 2738–2745.

Ullman, S. 1979 The interpretation of structure from motion. *Proceedings of the Royal Society of London. Series B. Biological Sciences* **203** (1153), 405–426.

Wallace, L., Lucieer, A., Watson, C. & Turner, D. 2012 Development of a UAV-LiDAR system with application to forest inventory. *Remote Sensing* **4** (6), 1519–1543.

Wang, R. 2013 3D building modeling using images and LiDAR: A review. *International Journal of Image and Data Fusion* **4** (4), 273–292.

Wang, L. & Yu, J. 2012 Modelling detention basins measured from high-resolution light detection and ranging data. *Hydrological Processes* **26** (19), 2973–2984.

Webster, T. L. & Dias, G. 2006 An automated GIS procedure for comparing GPS and proximal LiDAR elevations. *Computers & Geosciences* **32** (6), 713–726.

Westaway, R. M., Lane, S. N. & Hicks, D. M. 2000 The development of an automated correction procedure for digital photogrammetry for the study of wide, shallow, gravel-bed rivers. *Earth Surface Processes and Landforms: The Journal of the British Geomorphological Research Group* **25** (2), 209–226.

Westoby, M. J., Brasington, J., Glasser, N. F., Hambrey, M. J. & Reynolds, J. M. 2012 'Structure-from-motion' photogrammetry: A low-cost, effective tool for geoscience applications. *Geomorphology* **179**, 300–314.

Woodget, A. S., Carbonneau, P. E., Visser, F. & Maddock, I. P. 2015 Quantifying submerged fluvial topography using hyperspatial resolution UAS imagery and structure from motion photogrammetry. *Earth Surface Processes and Landforms* **40** (1), 47–64.

Yan, W. Y., Shaker, A. & El-Ashmawy, N. 2015 Urban land cover classification using airborne LiDAR data: A review. *Remote Sensing of Environment* **158**, 295–310.

Zhao, G., Balstrøm, T., Mark, O. & Jensen, M. B. 2021 Multi-scale target-specified sub-model approach for fast large-scale high-resolution 2D urban flood modelling. *Water* **13** (3), 259.

Zhao, G., Mark, O., Balstrøm, T. & Jensen, M. B. 2022 A sink screening approach for 1D surface network simplification in urban flood modelling. *Water* **14** (6), 963.